Chemical Physics Letters 577 (2013) 114–120

Contents lists available at SciVerse ScienceDirect

Chemical Physics Letters

journal homepage: www.elsevier.com/locate/cplett

# Experimental and theoretical approach of nanocrystalline $TiO_2$ with antifungal activity

Valeria M. Longo [a,*], Francini C. Picon [a], Camila Zamperini [a], Anderson R. Albuquerque [b], Julio R. Sambrano [b], Carlos E. Vergani [a], Ana L. Machado [a], Juan Andrés [c], Antônio C. Hernandes [d], José A. Varela [a], Elson Longo [a]

[a] INCTMN, Universidade Estadual Paulista, P.O. Box 355, CEP 14801-907 Araraquara, SP, Brazil
[b] Grupo de Simulação Molecular, Universidade Estadual Paulista, P.O. Box 477, CEP 17033-360 Baurú, SP, Brazil
[c] Departament de Química Física i Analítica, Universitat Jaume I, Campus de Riu Sec, Castellon E12080, Spain
[d] INCTMN, Universidade de São Paulo, Instituto de Física de São Carlos, USP, 13560-970 São Carlos, SP, Brazil

ARTICLE INFO

*Article history:*
Received 28 February 2013
In final form 21 May 2013
Available online 1 June 2013

ABSTRACT

Using a solvothermal method for this research we synthesized nanocrystalline titanium dioxide (nc-$TiO_2$) anatase particles with a mean diameter of 5.4 nm and evaluated their potential antifungal effect against planktonic cells of *Candida albicans* without UV radiation. To complement experimental data, we analyzed structural and electronic properties of both the bulk and the (1 0 1) surface of anatase by first-principles calculations. Based on experimental and theoretical results, a reactive $O_2H^*$ and $OH^*$ species formation mechanism was proposed to explain the key factor which facilitates the antifungal activity.



## 1. Introduction

Nanocrystalline $TiO_2$ (nc-$TiO_2$) is a modern photoactive material [1] with a wide range of possible applications such as solar cells [2], self-cleaning fibers [3], pollutant removal [4], sunscreen [5], water splitting [6] and antifungal activity by photokilling [7].

Typically, $TiO_2$ has three crystalline phases: anatase, rutile and brookite, anatase exhibits high stability and high photocatalytic activity. Anatase $TiO_2$ belongs to a tetragonal lattice ($I4_1/amd$), where the Ti atoms are sixfold-coordinated by O atoms, and O atoms are threefold-coordinated by Ti atoms. The most thermodynamically stable surface (1 0 1) has five and sixfold-coordinated Ti ($Ti_{5c}$ and $Ti_{6c}$) and two and three-coordinated O ($O_{2c}$ and $O_{3c}$) sites [8].

Technical-grade $TiO_2$ is very often supplied in the anatase form; most $TiO_2$ nanomaterials are produced in the anatase form, and in most cases, anatase is reported to be photocatalytically more active than rutile [9]. This lack of experimental data on anatase single-crystal surfaces is mostly due to the limited availability of anatase crystals of sufficiently large size [10]. This discrepancy has motivated several theoretical investigations of anatase [11,12], but clearly is lack of experimental data in the literature regarding well-defined anatase surfaces that could enable verification of these theoretical predictions.

As particle dimensions reduce towards the nanoscale, the surface-to-volume ratio proportionally increases, and small-size effects associated with nanoparticles become more pronounced [13]. Understanding the nanoscale topography of surface sites such as terraces, steps, kinks, adatoms and vacancies, and their effects on catalytic and other physico-chemical properties is the key to designing nanoscale functional materials by nanotechnology [13]. Many features of the material no longer remain constant but become tunable with size. As a consequence, nanoparticles with increased surface-to-volume ratio are expected to be more reactive due to the dominance of the undercoordinated atoms; i.e. broken bonds and nonbonding electrons at the nanoscale [14]. Thus, following the seminal sentence of Pauli: "God made the bulk; surfaces were invented by the devil", very recently, Mudunkotuwa and Grassian [15] emphasized the impact of surface structure and surface energetics on the environmental behavior of nanomaterials. Bacterial contamination and growth in water are potential health hazards requiring disinfection. Therefore the use of inorganic antimicrobial agents rather than organics has attracted interest due to improved safety and stability [16] and ceramics with inherent antifungal activity are convenient to use as they are insoluble.

Research reports have appeared concerning the antimicrobial effects of $TiO_2$ powder [17,18], often referring to $OH^*$ as the toxic agent. However, doubt remains about the actual antimicrobial agents because several active oxygen species other than $OH^*$ are generated by photocatalytic reactions; e.g. superoxide anions ($O_2^{\prime}$), perhydroxyl radicals ($HOO^{\cdot}$) and hydrogen peroxide ($H_2O_2$) which are all formed on the surface of the photocatalyst [19]. These species are better known for their role in biological reactions [20] than in the decomposition of ordinary organic molecules. In addition, microorganisms can act as powerful probes to investigate these active oxygen species. Since microorganisms are much larger

* Corresponding author.
*E-mail address:* valerialongo@liec.ufscar.br (V.M. Longo).

0009-2614/$ - see front matter © 2013 Published by Elsevier B.V.
http://dx.doi.org/10.1016/j.cplett.2013.05.056

than single molecules, the photocatalytic antimicrobial effect necessarily involves long-range interactions between the reactants (microorganisms) and the photocatalyst. These interactions are usually neglected in photocatalytic reactions which are typically surface reactions for ordinary molecules [21].

The inactivation of microbial cells is important in medical and bio-industrial fields. Recently, there has been a considerable increase in the incidence of fungal infections in humans, including superficial and systemic infections, which have been associated with the wide use of immunosuppressive therapies and broad-spectrum antibiotics, among other factors. Particularly, the antifungal effect of the nc-$TiO_2$ solution against *Candida albicans* is relevant because this yeast is most isolated from human infections, mainly in immunocompromised patients [22]. $TiO_2$-based photocatalysis produces reactive oxygen species responsible for the peroxidation of phospholipid components of the cell outer membrane [23]. The lipid peroxidation increases the cell permeability and permits the efflux of intracellular contents which eventually causes cell death [23].

To date no comprehensive study has been conducted on the relationship between the nc-$TiO_2$ chemical composition, size, shape, crystalline structure as well as their toxicological effects and adsorption or absorption with microorganisms. Thus conditions where nc-$TiO_2$ acts as a bactericide as well as the corresponding mechanism remains a subject for investigation. To address these questions, a potentially sensitive fungal *C. albicans* has been selected.

In this research, using a solvothermal process [24], we synthesized nc-$TiO_2$ anatase particles with mean diameter of 5.4 nm and evaluated their potential antifungal effect against planktonic cells of *C. albicans* without UV light. The nc-$TiO_2$ was structurally characterized by X-ray diffraction (XRD), FT-Raman spectroscopy and high-resolution transmission electron microscopy (HR-TEM). Due to difficulties in assigning correct electronic responses at an atomistic resolution, the key factor in governing the antifungal activity in nc-$TiO_2$ is still unclear. Fortunately, first-principles simulations can fundamentally extend our ability to understand electronic properties at atomic-scale resolution. Thus, to complement experimental data, the bulk and (101) surfaces of anatase were evaluated by first principles calculations. In light of these results, an antifungal effect mechanism was formulated by the formation of reactive oxygen species.

## 2. Synthesis, experimental techniques and antimicrobial measurements

The typical synthesis procedure can be described as follows: 500 mL of isopropanol ($(CH_3)_2CHOH$) (99.5% purity, Tédia) and 12.5 g of acetylacetone ($C_5H_8O_2$) ($\geqslant$98%, Fluka) were mixed: 7.10 g of titanium isopropoxido ($Ti[OCH(CH_3)_2]_4$) (97% purity, Aldrich) was added to this solution under constant agitation and at ambient temperature. A transparent yellow solution formed which is a characteristic of a titanium and acetylacetone complex. Then 5.0 mL of an acid solution of water with nitric acid ($H_2NO_3$) (70% purity, Synth) 1 M was added to the yellow solution to produce alkoxide hydrolysis. This solution was then heated at 60 °C for 24 h which resulted in an intense transparent yellow colloid. Then the mixture was transferred into a Teflon autoclave which was sealed and processed by a solvothermal method. Temperature was maintained at 120 °C for 6 h; the pressure in the autoclave was stabilized at 294 kPa. After the solvothermal treatment, the autoclave was cooled to room temperature. The sovothermal process lead to nanoparticules in suspension. After this, the solution was centrifuged, washed several times and dried at 40 °C. Thereafter, an aqueous solution of nc-$TiO_2$ (2 mg/mL) was prepared for the microbiological tests.

nc-$TiO_2$ was characterized by different techniques. XRD was carried out on the as-prepared sample to determine the structural characteristics of the obtained phase (Rigaku DMax 2500PC). FT-Raman spectroscopy was recorded with a Bruker-RFS 100 (Germany). Spectra in the range from 50 to 1000 $cm^{-1}$ were obtained using a 1064 nm line of a Nd:YAG laser with its maximum output power maintained at 100 mW. The morphology and size of the particles were investigated by using TEM (Jeol 3010) and HR-TEM (Jeol 3010). All measurements were taken at room temperature.

The antifungal property of nc-$TiO_2$ solution was evaluated against *C. albicans* ATCC 90028. Initially, *C. albicans* was plated in SDA (Sabouraud dextrose agar) and incubated for 48 h at 37 °C. Then one loopful of *C. albicans* was inoculated in 5 ml of RPMI-1640 culture medium and incubated in an orbital shaker at 75 rpm, for 21 h at 37 °C [25]. Cells of the resultant culture were separated by centrifugation at 4000 rpm for 5 min, washed twice with phosphate-buffered saline (PBS: pH 7.2) and resuspended in 5 ml of RPMI-1640 medium. Experiments were performed on 96-well microdilution plates with a final volume of 200 μL/well. For experimental wells, aliquots of 100 μL of *C. albicans* at concentration of $1 \times 10^4$ colony-forming units (CFU/mL) were incubated in 100 μL nc-$TiO_2$ solution (2 mg/mL) for 24 h at 37 °C. Hence, the final *C. albicans* concentration in each well was $5 \times 10^3$ colony-forming units (CFU/mL), and the final nc-$TiO_2$ solution concentration was 1 mg/mL. For control wells, 100 μL of *C. albicans* at concentration of $1 \times 10^4$ colony-forming units (CFU/mL) were incubated in 100 μL of RPMI-1640 culture medium for 24 h at 37 °C. After the incubation period, aliquots of 100 μL from the wells (control and experimental) were diluted ($10^{-1}$, $10^{-2}$, $10^{-3}$ and $10^{-4}$) in PBS, inoculated on SDA (in duplicate) and cultured at 37 °C for a period for 48 h. The number of colony-forming units per milliliter (CFU/mL) was calculated and log10 transformed; experiments were carried out in triplicate on three different occasions.

## 3. Theoretical procedures

The best accuracy on first-principles calculations in solid state is a requirement to simulate structural and electronic properties of bulk, surfaces and your defects, such as vacancy and impurities.

The computational simulation was performed under the framework of the periodic density functional theory (DFT) using the CRYSTAL09 computer code [26]. In particular, our group has employed this theory for studies of $TiO_2$ [27,28] and recently reported a $TiO_2$ anatase new study with better results when compared with conventional DFT/B3LYP methodology [29].

For improved the accuracy on simulations, weakly interaction as dispersive energies can be taken into account. Conventional DFT methods require the inclusion of semiempirical terms to describe these phenomena. DFT augmented with an empirical dispersion term to pure Khon-Sham DFT energy (DFT-D) has demonstrated high accuracy in many different applications [30] leading to a closer agreement with experimental data.The general form of total energy in the DFT-D method is given by $E_{\text{DFT-D}} = E_{\text{KS-DFT}} + E_{\text{disp}}$ where $E_{\text{KS-DFT}}$ is the usual self-consistent Kohn–Sham energy from the arbitrary density functional and $E_{\text{disp}}$ is a semi-empirical dispersion term. This methodology was recently employed on bulk $TiO_2$ anatase description by DFT/B3LYP-D* [29].

The conventional unit cell of $TiO_2$ anatase phase is defined by three crystallographic parameters: $a$, $c$ and the internal coordinate $u$ ($u = d^{\text{ap}}_{\text{Ti–O}}/c$, where $d^{\text{ap}}_{\text{Ti–O}}$ is the apical Ti–O bond length). The total energy minimization with respect to cell parameters and the internal coordinate $u$ was conducted with the standard 6-31G* and 6-21(d-31)G for oxygen and titanium, respectively.

The calculated optimized B3LYP-D* and experimental values [31,32] (in parentheses) for $a$, $c$ and the internal parameter $u$ are: $a = 3.7875$ (3.78512) Å; $c = 9.5146$ (9.51185) Å and $u = 0.2082$ (0.208) which are in good agreement with experimental and theoretical lattice parameters. From the optimized bulk structure, we built a symmetrical 2D slab model (finite in the $z$-direction but periodic in the $x$ and $y$-direction). Because the number of layers plays a significant role in the accuracy of the calculations, we selected the slab model size as a surface energy function [33]. First, we calculated surface energy values as a function of slab thickness, and the results show that convergence is achieved when a 15-layer slab is used; this model is an appropriate system to study the geometry and the electronic structure of the (1 0 1) surface.

HR-TEM images analysis reveals that the most stable, and thus, the predominant anatase surface is (1 0 1); therefore, two theoretical models were derived: (1) from the optimized bulk model; and (2) from the (1 0 1) anatase surface. This modeling and simulation facilitated a simple scheme to comprehend of the simultaneous bulk and surface effects in the resultant electronic structure of nc-$TiO_2$; i.e., this theoretical scheme is appropriate to represent the mismatch between bulk and surface electronic structures as a key factor revealing the fungistatic effect which appears only when the nanoscale is reached.

Figure 1 is a pictorial view of the bulk and (1 0 1) anatase crystallographic surface which exposes both fivefold $Ti_{5c}$ and sixfold $Ti_{6c}$ coordinated Ti atoms and twofold $O_{2c}$ and threefold $O_{3c}$ coordinated O atoms. The surface has an O–Ti–O motif where each Ti layer has adjacent O layers above and below the Ti plane. The surface also contains channels oriented along the [0 1 0] direction.

The (1 0 1) surface can have two different terminations: a titanium fourfold-coordinated, $Ti_{4c}$ or a fivefold-coordinated $Ti_{5c}$ with a twofold-coordinated oxygen atom $O_{2c}$. The $Ti_{5c}$ termination is more stable than the $Ti_{4c}$ termination, and consequently, the $Ti_{5c}$ termination surface is selected as a model for our analysis; deep $Ti_{6c}$ and $O_{3c}$ are also included this model. The $TiO_2$ bulk and (1 0 1) surface band structure were constructed along the appropriate high-symmetry paths of the corresponding irreducible Brillouin zone.

## 4. Results and discussion

XRD patterns of synthesized $TiO_2$ indicate crystalline single phase nanocrystals with a tetragonal anatase $TiO_2$ structure and a space group of $I4_1/amd$ in a $D_{4h}^{19}$ symmetry (PDF number 21–1272) (see Figure 2). The peaks are broad which is an indication of the structural disorder of the material which is a consequence of the surface structure that is different from the bulk structure. This difference occurs because there is a 'break' in the crystalline

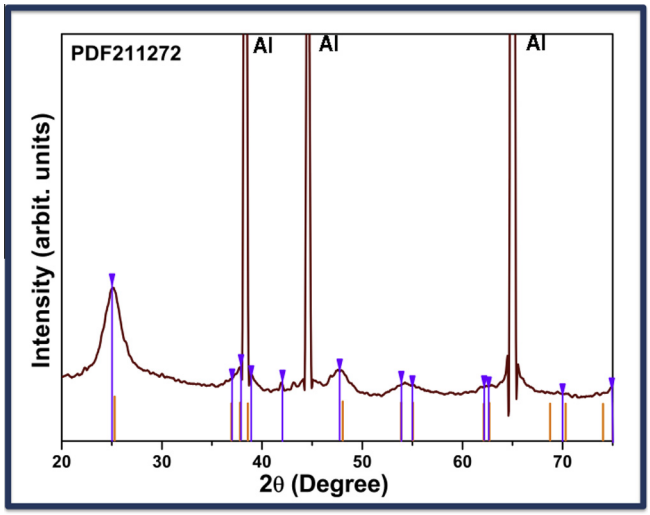


**Figure 2.** $TiO_2$ anatase phase XRD pattern with a PDF number 21-1272.

atom arrangement in the ending surface. In this way, in surface there are less coordinated atoms with breaking bonds. This peculiarity renders a more disordered characteristic to the surface than from the bulk. This means that the bulk and surface are crystalline, but the XRD reflects a mix between two different structures. In the case of a nanostrutured material, the surface effect in relation to the bulk effect is more important as the particle size is reduced [34]. The mismatch between the bulk and surface structure results in significant properties in nanomaterials.

The anatase structure has 3 acoustic modes and 15 optical modes. Among the optical modes, the irreducible representations are $1A_{1g} + 1A_{2u} + 2B_{1g} + 1B_{2u} + 3E_g + 2E_u$. Representations with the subscript $u$ are IR-active, while representations with the subscript $g$ are R-active; the $B_{2u}$ mode is silent.

Figure 3 shows the $TiO_2$ FT-Raman spectrum which is similar to the anatase bulk structure, with the exception of their blueshift frequency. $TiO_2$ nanoparticles have frequently been investigated with Raman spectroscopy because of the unusual band broadening and shifts of Raman bands with decreasing particle size [35,36]. Xu et al. [36] have tried to explain the variation in the Raman bands with a phonon confinement model; however, there is no general agreement about the origin of the broadening and shifts of Raman bands.

Raman lines at 151, 200, 409, 515 and 633 $cm^{-1}$ can be assigned as $E_g$, $E_g$, $B_{1g}$, $A_{1g}$ or $B_{1g}$, and $E_g$ modes of the anatase phase, respectively. As recently, pointed out by theoretical calculations the

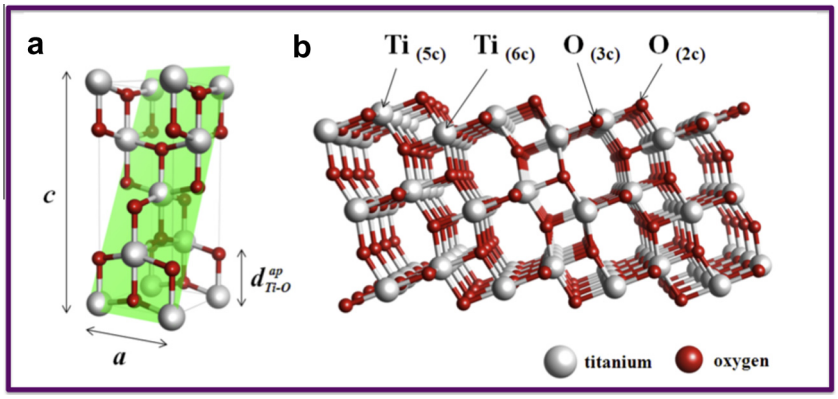


**Figure 1.** a) Conventional $TiO_2$ anatase unit cell; and b) (1 0 1) $TiO_2$ anatase surface.

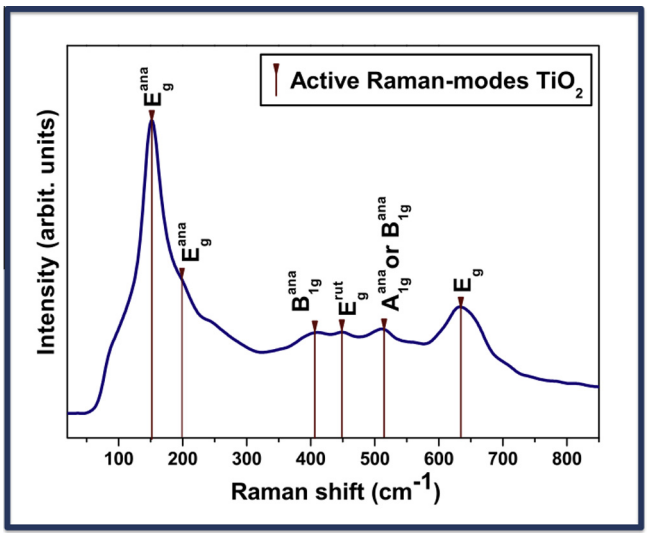


**Figure 3.** FT-Raman modes of a $TiO_2$ anatase phase with a slight amount of a rutile phase.

515 $cm^{-1}$ line is a $B_{1g}$ mode [29]. The slight 449 $cm^{-1}$ line in the spectrum can be assigned as a $TiO_2$ rutile phase (P42/m nm tetragonal space group) which does not appears in the XRD analysis. Thus the slight among of $TiO_2$ in the rutile form in the synthesized $TiO_2$ is evident. The strongest $E_g$ mode at 151 $cm^{-1}$ arising from the external vibration of the anatase structure is resolved which indicates that an anatase phase was formed in the $TiO_2$ nanocrystals, and short-range order was reached. This conclusion is consistent with XRD results shown in Figure 2. XRD usually reveals the long-range order of materials and gives average structural information within several unit cells. Raman scattering as a local probe is very sensitive to the crystallinity and microstructures of materials. Raman lines become weak and broad when the samples have local lattice disorders. High-frequency nanocrystalline Raman lines exhibit a weak and overlapped feature which XRD measurements confirms as surfaces disorders (Figure 3).

A TEM micrograph, Figure 4a, shows that nc-$TiO_2$ structures have an apparent homogenous and spherical morphology. A histogram of analysis of 200 particles obtained using ImageJ software (http://rsbweb.nih.gov/ij/) is depicted in the Figure 4b and shows that the nanocrystalline particle size distribution has a mean diameter of 5.4 nm.

A HR-TEM micrograph, Figure 4c, shows that nc-$TiO_2$ particles are crystalline with an interplane distance of 0.35 nm which corresponds to the (1 0 1) plane of the anatase phase, these morphologies are formed by an OA (oriented attachment) mechanism. In this nonclassical crystallization process, the crystal formation, which is controlled by a monomer-by-monomer assembly, is replaced by a process involving the spontaneous self-organization of adjacent nanocrystals to share a common crystallographic orientation and coalescence; i.e., by the OA growth mechanism [37]. A kinetic model to describe the OA growth process of nanoparticles in colloidal suspensions was proposed [38] and other studies based on this mechanism were developed by Penn [39] and Xu et al. [40].

Microbiological tests showed that the exposure of *C. albicans* to the nc-$TiO_2$ solution resulted in a 30% reduction in fungal growth as compared with growth control for a decrease from 8.29 log 10 CFU/mL to 5.83 log 10 CFU/mL. This result indicates that the nc-$TiO_2$ solution has an antifungal effect against *C. albicans* cells even without light-induced radiation. These results are depicted in Table 1.

Theories about the microbial activity of $TiO_2$ are dependent on the light-induced reactivity of the $TiO_2$ photo-catalyst with water produces active species such as hydroxyl radicals, superoxides and hydrogen peroxide [41,42]. Gurr et al. [43] demonstrated that small (10–20 nm) $TiO_2$ particles also induce lipid peroxidation, micronuclei formation as well as increased hydrogen peroxide and nitric oxide production in a human bronchial epithelial cell line even in the absence of photoactivation. More recent studies

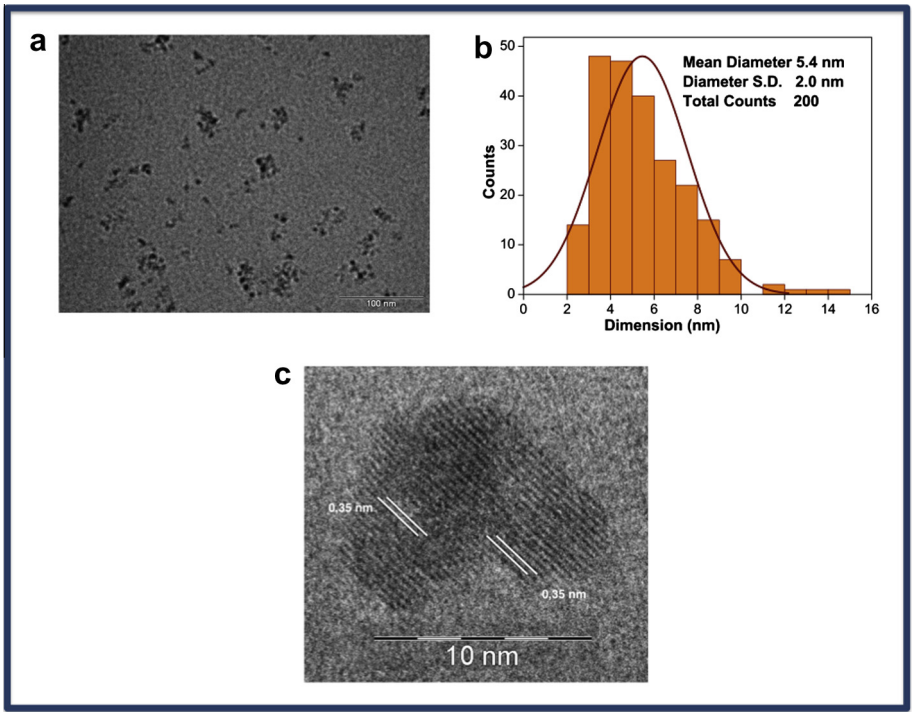


**Figure 4.** (a) Typical TEM micrographic of the nc-$TiO_2$ distribution; (b) Size distribution histogram indicating the mean size with respect to the standard deviation for a total count of 200 particles and; (c) HR-TEM micrographic of nc-$TiO_2$ particles in apparent oriented attachment (OA) growth in the [1 0 1] direction.

**Table 1**
Differences between control and nc-$TiO_2$ solution against *C. albicans* cells.

| | Growth condition | |
|---|---|---|
| | Control | nc-$TiO_2$ solution |
| *Occasion* ($n$ = 3) | | |
| 1st | 6.71 | 4.61 |
| 2nd | 9.15 | 6,60 |
| 3rd | 9.00 | 6.28 |
| Mean (± standard deviation) | 8.29 (1.19) | 5.83 (0.95) |

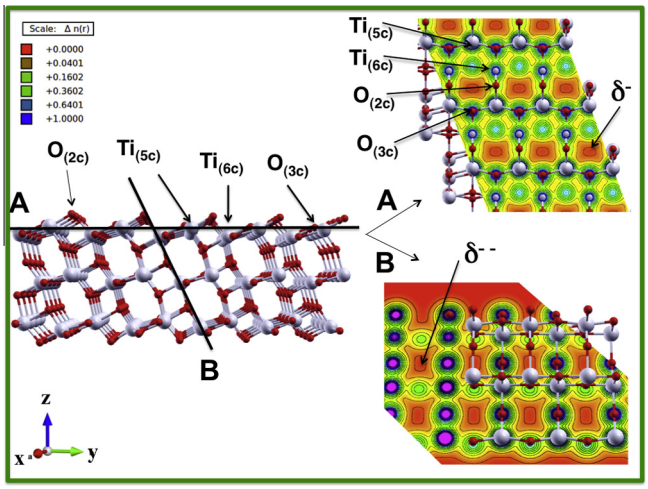


**Figure 5.** Electron density maps of the (101) surface projected on A and B planes.

reveal that ultrafine titania nanoparticles can also affect cell-matrix adhesion in keratinocytes for extracellular matrix remodeling (again in the absence of illumination) [44], and fiber shaped particles can induce inflammation activation and release of inflammatory cytokines through a cathepsin B-mediated mechanism [45].

A number of research groups have analyzed titania surface reactions [46], however, a basic understanding remains elusive. Therefore, in this study we established both relaxed (101) surface and bulk of $TiO_2$ anatase to elucidate this phenomenon by assuming that these reactions occur at under-coordinated cationic Ti surface sites and that the reaction efficiency is directly proportional to the number of active site in a given sample [47]. First, we analyzed the electron charge density maps for the anatase (101) surface, Figure 5; chosen planes for the analysis are denoted as A and B.

In the A plane, the covalent bonding nature of Ti-O decreases as a consequence of the asymmetric $Ti_{(5c)}$ that can be represented as the complex cluster $[TiO_5 \cdot V_O^x]_S$ where the Kröger-Vink notation is used, and the sub index S represents the surface. This breaking symmetry process yields a charge separation; i.e., a polarization between $[TiO_6]_S^x$ and $[TiO_5 \cdot V_O^x]_S$ complex clusters. Plane B clearly shows that the bonding between Ti and O is covalent and is visible due to hybridization between the O (2p) states and the Ti (3d) states in the $[TiO_6]_S^x$ complex cluster. The differences between plane A (more related to the surface) and plane B (more related to the bulk) show a globally unbalance charge distribution between bulk and surface. In this way, the plane A surface are more positively charged than plane B.

Figure 6 depicts the calculated band structure, and densities of state projected on atoms and the main corresponding bulk and (101) surface anatase orbitals.

A bulk band structure analysis shows that the band gap has an indirect transition of 3.55 eV which is located at the valence band (VB) ~ X point and at the conduction band (CB) $\Gamma$ point (see Figure 6a); this result is in good agreement with experimental data, of 3.51 eV [48].

The density of states for the bulk shows that the uppermost VB is formed by 2p oxygen atom orbitals with a small contribution of Ti 3d orbitals. The CB consists mainly of 3d Ti atom orbitals with a smaller contribution of 2p O atom orbitals (see Figure 6b).

Figure 6c depicts the (101) surface band structure with an indirect band gap of 4.03 eV between the VB K′ and the CB Γ point. An atomic orbital contributions analysis shows that the top of the VB

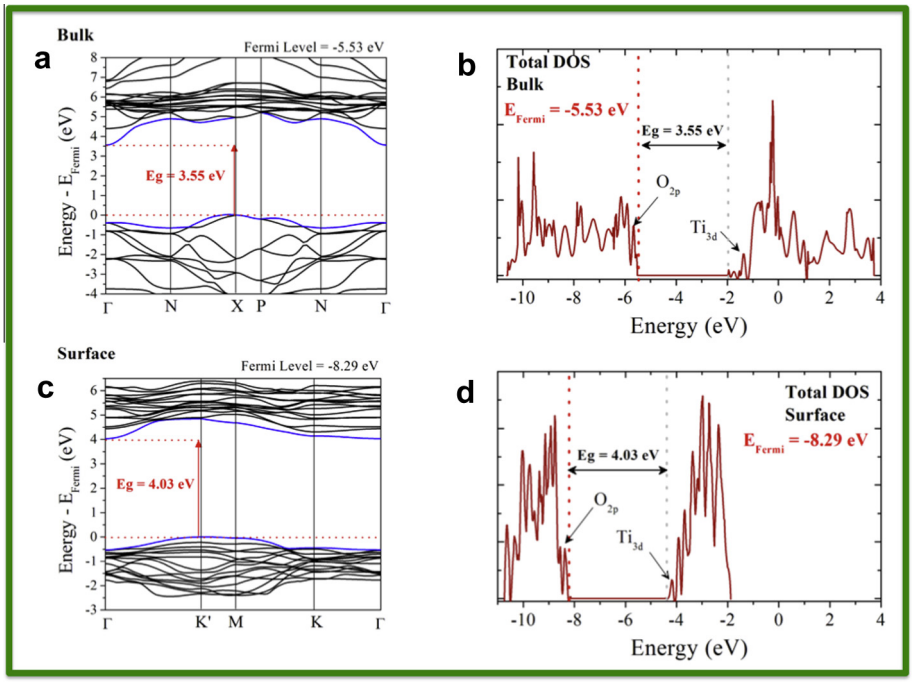


**Figure 6.** Calculated energy band structures for (a) bulk SZ-o and (c) (101) surface as well as total density of states for (b) the bulk and d) the (101) anatase surface.

consists mainly of non-bonding 2p orbitals belonging to O surface atoms, especially $2p_x$ orbitals (see Figure 6d).

The as-prepared nc-$TiO_2$ has a mean size of ~5 nm (50 Å), and the constructed surface model has a mean size of ~25 Å. Thus the mismatch between the bulk and the surface in this scale of size dictates the final electronic crystalline structure. This structure is dependent upon the interaction between the bulk/surface and the surface/bulk in a dynamic process that relies on many factors such as order–disordered effects [41], morphology, size as well as the chemical environment and the temperature [49].

Based on both experimental and theoretical results we propose a model where the driving force of this dynamic process is the order–disordered effect at the intermediate range as experimentally confirmed by the broadening peaks observed in XRD and Raman spectra in nc-$TiO_2$. Additionally, the bulk and the surface are neutral with the same relevance in terms of the electronic structure.

Light-induced ionization over the band gap which induces electron–hole pair formation may be represented by the following reaction:

$$h\nu \rightarrow e' + h^{\cdot}$$

Figure 7 illustrates a possible antimicrobial effect mechanism by using nc-$TiO_2$ in the absence of light-induced radiation as the $e'$ and $h^{\cdot}$ are present in the surface of nc-$TiO_2$ as discussed in the charge density maps of Figure 5.

This activity is closely related to energy level alignment; in the first step, electrons split from the electron bulk Fermi level $(E_{Fe})_B$ to the electron surface Fermi level $(E_{Fe})_S$ and holes split from the hole bulk Fermi level $(E_{Fh})_B$ to the hole surface Fermi level $(E_{Fh})_S$. These dynamic Fermi levels and are a spontaneous process as the electronic surface structure has the electron and hole Fermi energies located at 2.76 and 2.28 eV, respectively, which is bellow the CB and VB of the bulk.

The activity is determined by the behavior of photogenerated holes. A hole in the acceptor state $(E_{Fh})_B$ and an electron in the donor state $(E_{Fe})_B$ split into the acceptor state $(E_{Fh})_S$ and donor state $(E_{Fe})_S$, respectively, according to the following equations:

$$[TiO_6]^x_B - [TiO_5 \cdot V^x_O]_S \rightarrow [TiO_6]'_B - [TiO_5 \cdot V^{\cdot}_O]_S \quad (1)$$

$$[TiO_6]^x_B - [TiO_6]^x_S \rightarrow [TiO_6]^{\cdot}_B - [TiO_6]'_S \quad (2)$$

where $[TiO_6]'_B$ and $[TiO_6]'_S$ are donors and $[TiO_5 \cdot V^{\cdot}_O]_S$ and $[TiO_6]^{\cdot}_B$ are acceptors.

Thus the interaction between the bulk and the surface promotes trapped e' and *h*. pairs without light-induced radiation.

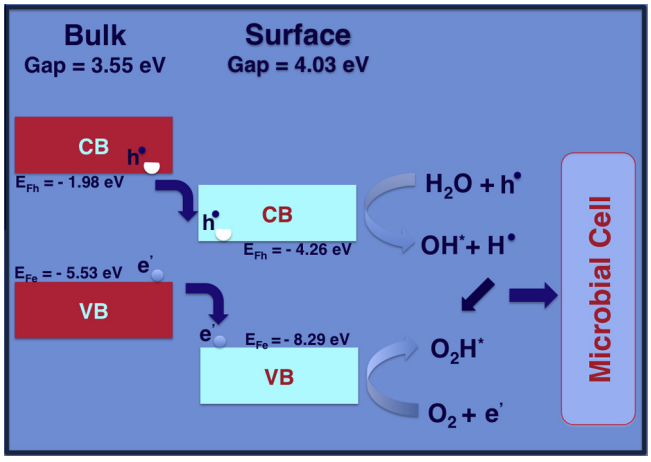


**Figure 7.** Possible antimicrobial effect mechanism by using nc-$TiO_2$ in the absence of light-induced radiation.

In a second step the surface interacts with $H_2O$ or/and $O_2$ depending on the chemical environment:

$$[TiO_6]'_B - [TiO_5 \cdot V^{\cdot}_O]_S + H_2O \rightarrow [TiO_6]'_B - [TiO_5 \cdot V^x_O]_S ... HO^*_{(ads)} + H^{\cdot} \quad (3)$$

$$[TiO_6]^{\cdot}_B - [TiO_6]'_S + O_2 \rightarrow [TiO_6]^{\cdot}_B - [TiO_6]^x_S .... O'_{2(ads)} \quad (4)$$

$$[TiO_6]^{\cdot}_B - [TiO_6]^x_S ... O'_{2(ads)} + H^{\cdot} \rightarrow [TiO_6]^{\cdot}_B - [TiO_6]^x_S ... O_2H^*_{(ads)} \quad (5)$$

The $OH^*$ and $HO^*_2$ radicals generated at the $TiO_2$ surface will indiscriminately attack cell wall polysaccharides, membrane lipids and membrane proteins whose integrity is critical for cellular survival. The abundance and peripheral location of the cell envelope polysaccharides mark them as the first target, and only after this barrier has been breached can the highly reactive radicals directly attack the cell membrane, whose integrity is critical for cellular survival. The cell membrane is not only the ultimate barrier between the environment and the cell interior, but is also critical for the function of membrane- associated proteins [50].

From a theoretical point of view, there is an reasonable agreement between theoretical and experimental data. However discrepancies could occur because computational models consider the system as a perfect crystal with no defects (order–disorder, vacancy and impurities), which could lead to deviations when compared with the results obtained experimentally. In this way, we shall consider that these variables might interfere with the values obtained experimentally. Considering these effects, the current results, might offer preliminary guidance for the microbial effect.

## 5. Conclusions

The control of particle size and morphology promotes modulation of advanced properties in nano-oxide materials that can be used in future novel technologies which can in principle explore materials unavailable in the bulk single crystal form; however their importance is dramatically dependent upon surface-interface states.

In this study nc-$TiO_2$ particles of approximately 5.4 nm diameter were successful synthesized by using a solvothermal system. The particle morphology and size were evaluated by HR-TEM, and the preponderant anatase phase was identified by XRD and FT-Raman analysis. The blue shift in the FT-Raman analysis was attributed to the confinement effect due to the particle size. Microbiological tests demonstrated that the nc-$TiO_2$ possesses anti-candidal activity without light-induced radiation.

Using first-principles calculations, the bulk and (1 0 1) anatase surface were evaluated, and we propose that reactive $OH^*$ and $HO^*_2$ species formation occurs at the nc-$TiO_2$ surface. The mismatch between bulk and surface electronic properties is proposed as the possible key factor which promotes the synthesized nc-$TiO_2$ antimicrobial effect. This conclusion supports the significance of bond deficiency and bond enhancement at surfaces; i.e. the Ti–O surface broken bond is the essential cause for the formation of reactive $OH^*$ and $HO^*_2$ species at surface and spontaneous band gap shift.

Results of this research provide fundamental insight into the role of surface/bulk defects in antimicrobial activity and reveal a novel strategy for significantly improving this activity by controlling surface/bulk defects. We believe that this process may also be applicable for other materials such as ZnO, $SnO_2$, etc.

## Acknowledgments

The authors are thankful for the financial support of the following Brazilian research financing institutions: CAPES, CNPq, and

FAPESP and by Generalitat Valenciana for *Prometeo*/2009/053 project, Programa de Cooperación Científica con Iberoamerica (Brasil), *Ministerio de Educación* (PHB2009-0065-PC). Computer facilities were supported by resources supplied by the Molecular Simulation Laboratory and the Center for Scientific Computing of the São Paulo State University.

## References

[1] A. Fujishima, K. Honda, Nature 238 (1972) 37.
[2] W.Q. Peng, M. Yanagida, L.Y. Han, S. Ahmed, Nanotechnology 22 (2011).
[3] W.S. Tung, W.A. Daoud, J. Mater. Chem. 21 (2011) 7858.
[4] A.Y. Zhang, M.H. Zhou, L. Han, Q.X. Zhou, J. Hazard. Mater. 186 (2011) 1374.
[5] C. Botta et al., Environ. Pollut. 159 (2011) 1543.
[6] H.J. Yun, H. Lee, J.B. Joo, N.D. Kim, J. Yi, J. Nanosci. Nanotechnol. 11 (2011) 1688.
[7] F. Haghighi, S.R. Mohammadi, P. Mohammadi, M. Eskandari, S. Hosseinkhani, Med. J. 113 (2012) 707.
[8] U. Diebold, Surf. Sci. Rep. 48 (2003) 53.
[9] O.O. Prieto-Mahaney, N. Murakami, R. Abe, B. Ohtani, Chem. Lett. 38 (2009) 238.
[10] Y.B. He, A. Tilocca, O. Dulub, A. Selloni, U. Diebold, Nat. Mater. 8 (2009) 585.
[11] A. Tilocca, A. Selloni, J. Phys. Chem. B 108 (2004) 19314.
[12] V.M. Sanchez, J.A. Cojulun, D.A. Scherlis, J. Phys. Chem. C 114 (2010) 11522.
[13] Z.Y. Zhou, N. Tian, J.T. Li, I. Broadwell, S.G. Sun, Chem. Soc. Rev. 40 (2011) 4167.
[14] C.Q. Sun, Nanoscale 2 (2010) 1930.
[15] I.A. Mudunkotuwa, V.H. Grassian, J. Environ. Monit. 13 (2011) 1135.
[16] W. Jiang, H. Mashayekhi, B.S. Xing, Environ. Pollut. 157 (2009) 1619.
[17] J.C. Ireland, P. Klostermann, E.W. Rice, R.M. Clark, Appl. Environ. Microbiol. 59 (1993) 1668.
[18] C. Wei et al., Environ. Sci. Technol. 28 (1994) 934.
[19] G.F. Fu, P.S. Vary, C.T. Lin, J. Phys. Chem. B 109 (2005) 8889.
[20] B. Halliwell, J.M.C. Gutteridge, Biochem. J 219 (1984) 1.
[21] Y. Kikuchi, K. Sunada, T. Iyoda, K. Hashimoto, A. Fujishima, J. Photochem. Photobiol. A Chem. 106 (1997) 51.
[22] F.N. Chen, X.D. Yang, Q. Wu, Build. Environ. 44 (2009) 1088.
[23] G. Gogniat, M. Thyssen, M. Denis, C. Pulgarin, S. Dukan, FEMS Microbiol. Lett. 258 (2006) 18.
[24] R.A. Roca, E.R. Leite, J. Am. Ceram. Soc. 96 (2013) 96.
[25] P.A. Wayne, CLSI (2008) Reference Method For Broth Dilution Antifungal Susceptibility Testing of Yeasts; Approved Standard in C.a.L.S. Institute (Ed.), 2008.
[26] R. Dovesi et al., CRYSTAL09 User's Manual, University of Torino, Torino, 2009.
[27] J.R. Sambrano, J.B.L. Martins, J. Andres, E. Longo, Int. J. Quantum Chem. 85 (2001) 44.
[28] A. Beltran, J.R. Sambrano, M. Calatayud, F.R. Sensato, J. Andres, Surf. Sci. 490 (2001) 116.
[29] A.d.R. Albuquerque, M.L. Garzim, I.M.G.d. Santos, V. Longo, E. Longo, J.R. Sambrano, J. Phys. Chem. A 116 (2012) 11731.
[30] M. Parac, M. Etinski, M. Peric, S. Grimme, J. Chem. Theory Comput. 1 (2005) 1110.
[31] C.J. Howard, T.M. Sabine, F. Dickson, Acta Crystallogr. Sect. B Struct. Sci. 47 (1991) 462.
[32] J.K. Burdett, T. Hughbanks, G.J. Miller, J.W. Richardson, J.V. Smith, J. Am. Chem. Soc. 109 (1987) 3639.
[33] A. Beltran, J. Andres, J.R. Sambrano, E. Longo, J. Phys. Chem. A 112 (2008) 8943.
[34] V.M. Longo et al., J. Phys. Chem. C 115 (2011) 5207.
[35] H.C. Choi, Y.M. Jung, S.B. Kim, Vib. Spectrosc. 37 (2005) 33.
[36] C.Y. Xu, P.X. Zhang, L. Yan, J. Raman Spectrosc. 32 (2001) 862.
[37] C. Burda, X.B. Chen, R. Narayanan, M.A. El-Sayed, Chem. Rev. 105 (2005) 1025.
[38] C. Ribeiro, E.J.H. Lee, E. Longo, E.R. Leite, ChemPhysChem 6 (2005) 690.
[39] R.L. Penn, J. Phys. Chem. B 108 (2004) 12707.
[40] X.X. Xu, F. Liu, K.H. Yu, W. Huang, B. Peng, W. Wei, ChemPhysChem 8 (2007) 703.
[41] T. Bak, J. Nowotny, N.J. Sucher, E. Wachsman, J. Phys. Chem. C 115 (2011) 15711.
[42] R. Nakamura, Y. Nakato, J. Am. Chem. Soc. 126 (2004) 1290.
[43] J.R. Gurr, A.S.S. Wang, C.H. Chen, K.Y. Jan, Toxicology 213 (2005) 66.
[44] K. Fujita et al., Toxicol. Lett. 191 (2009) 109.
[45] R.F. Hamilton, N.Q. Wu, D. Porter, M. Buford, M. Wolfarth, A. Holian, Part. Fibre Toxicol. 6 (2009).
[46] Y. Murakami, E. Kenji, A.Y. Nosaka, Y. Nosaka, J. Phys. Chem. B 110 (2006) 16808.
[47] T. Hirakawa, Y. Nosaka, Langmuir 18 (2002) 3247.
[48] L. Miao, S. Tanemura, P. Jin, K. Kaneko, A. Terai, N. Nabatova-Gabain, J. Cryst. Growth 254 (2003) 100.
[49] A.S. Barnard, A.I. Kirkland, Chem. Mat. 20 (2008) 5460.